Journal Pre-proofs

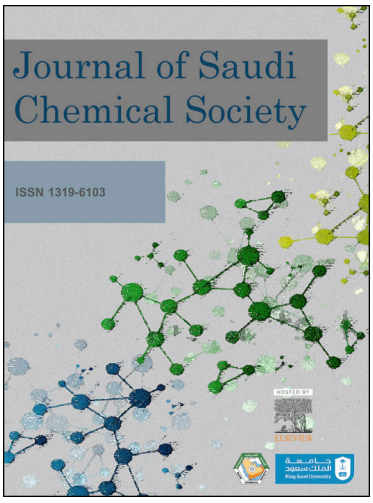

Original article

Optimizing the mechanical and surface topography of hydroxyapatite/Gd_2O_3/ Graphene oxide nanocomposites for medical applications

M.A. El-Morsy, Nasser S. Awwad, Hala A. Ibrahium, Walaa Alharbi, Mohammad Y. Alshahrani, A.A. Menazea

PII: S1319-6103(22)00045-X
DOI: https://doi.org/10.1016/j.jscs.2022.101463
Reference: JSCS 101463

To appear in: *Journal of Saudi Chemical Society*

Received Date: 7 January 2022
Revised Date: 19 March 2022
Accepted Date: 20 March 2022

Please cite this article as: M.A. El-Morsy, N.S. Awwad, H.A. Ibrahium, W. Alharbi, M.Y. Alshahrani, A.A. Menazea, Optimizing the mechanical and surface topography of hydroxyapatite/Gd_2O_3/Graphene oxide nanocomposites for medical applications, *Journal of Saudi Chemical Society* (2022), doi: https://doi.org/10.1016/j.jscs.2022.101463

Optimizing the mechanical and surface topography of hydroxyapatite/Gd_2O_3/Graphene Oxide nanocomposites for medical applications

M. A. El-Morsy[1, 2], Nasser S. Awwad[3], Hala A. Ibrahium[4, 5], Walaa Alharbi[6], Mohammad Y. Alshahrani[7], A. A. Menazea[8, 9, *]

[1]College of Science and Humanities in Al-Kharj, Physics Department, Plasma Technology and Material Science Unit, Prince Sattam Bin Abdulaziz University, Al-kharj 11942, Saudi Arabia
[2]Physics Department, Faculty of Science, University of Damietta, New Damietta 34517, Egypt
[3]Chemistry Department , Faculty of Science, King Khalid University, P.O. Box 9004, Abha 61413, Saudi Arabia.
[4]Biology Department , Faculty of Science , King Khalid University, P.O. Box 9004, Abha 61413, Saudi Arabia.
[5]Department of Semi Pilot Plant, Nuclear Materials Authority, P.O. Box 530, El Maadi, Egypt
[6]Department of chemistry, Science and Arts College, King Abdulaziz University , Rabigh, Kingdom of Saudi Arabia
[7]Department of Clinical Laboratory Sciences, College of Applied Medical Sciences, King Khalid University, P.O. Box 61413, Abha, 9088, Saudi Arabia
[8]Laser Technology Unit, Center of Excellent for Advanced Science, National Research Centre, Dokki, 12622, Giza, Egypt
[9]Spectroscopy Department, Physics Research Institute, National Research Centre, Dokki, 12622, Giza, Egypt

***Corresponding Author:** Dr. A. A. Menazea

E-mail: aanter7@gmail.com

Tel.: +201064260397

Acknowledgments

The authors extend their appreciation to the Deputyship for Research & Innovation, Ministry of Education in Saudi Arabia for funding this research work though the project number IFPKKU-2020/11.

Optimizing the mechanical and surface topography of hydroxyapatite/Gd_2O_3/Graphene Oxide nanocomposites for medical applications

Abstract

A ternary nanocomposite (TNC) was fabricated for introducing multifunctional properties for various biomedical applications. The nanocomposites consist of hydroxyapatite (HAP) combined with/without graphene oxide (GO) and gadolinium oxide (Gd_2O_3). The structural analysis was done using x-ray diffraction (XRD) and the hexagonal symmetry of HAP was detected besides the cubic crystal structure of Gd_2O_3. The lattice constants of HAP were around 9.4285 and 6.7476 Å, while for Gd_2O_3 was around 10.8441 Å. Further, the chemical investigation was done using Fourier transform infrared spectroscopy (FTIR), X-ray photoelectron spectroscopy (XPS), and Energy-dispersive X-ray spectroscopy (EDX) which confirmed the existence of all elements with a Ca/P ratio of 1.4. The morphological investigation detected the nanosheets of GO, and nanorods of HAP/ Gd_2O_3 with diameter and length decreased to 9.5 and 27 nm respectively. Moreover, the topological study based on a field emission scanning electron microscope (FESEM) showed that HAP/GO had the highest average roughness parameter (R_a) with around 4.8 nm, and the highest root mean square roughness value (R_q) with a value of 7 nm. Furthermore, the average pore size reached 7.99 nm for the NC of HAP/GO. In addition, the cumulative surface area using the density functional theory (DFT) method was calculated at around 44.61 m^2/g for TNC. The cell viability in vitro of human osteoblast cell line improved from 95.6 ± 0.6% to 96.7 ± 0.5% which indicates the biocompatibility of the implants to be used in biomedical applications.

Keywords: Gd_2O_3, Graphene oxide; Hydroxyapatite; Antibacterial; Cell viability.

1. Introduction

The critical-size bone defects which were formed due to trauma or injury can be considered as a hard challenge in orthopedics due to their requirement for surgical treatment [1, 2]. The surgical interventions in the present are often autografts or allografts [3]. The autograft is based on grafting a bone from the same patient but from a different place in the body [4]. Therefore, not all injuries can be autografted due to the low availability of some tissues in the human body in addition to the additional surgical site existence. On the other hand, the allografts are based on grafting tissues from another patient which is typically a donor [4]. Therefore, the immune system may reject the graft. Further, it might react sorely against the grafted tissues. Hence, designing a biodegradable material with multifunctional and desired properties can introduce a more flexible alternative solution. Nanocomposites (NCs) can be considered the most adaptable materials in the present day [5-8]. Therefore, they have a huge consideration among researchers due to their

important applications. The presence of nanomaterials in the composites made a broad interfacial area applicable with NCs compared to the conventional composites [9, 10]. That leads to improving the properties including mechanical, electrical, thermal, and biological properties [11]. NCs encourage a solution for bone tissue problems by replacing and repairing the damaged tissues. Moreover, the bone of a natural composite material contains an organic collagen matrix and an inorganic phase embedded in the matrix [12]. Many applications of nanomaterials have been reported in fine ceramics [13], catalytic [14-16], electrical [17-22], and sensors [23-25].

Hydroxyapatite (HAP) is the inorganic phase in the bone that can be easily synthesized in labs [26, 27]. Its similarity to bone composition leads HAP to have adequate biocompatibility and bioactivity for bone regeneration utilizations [4]. It is important to mention that around 70% of natural bone is nanocrystals hexagonal HAP symmetry [28]. The limitations of HAP lie in its brittleness, mechanical properties, poor antibacterial, and poor bioresorbability [29]. Shi et al. reported that they prepared HAP with different diameters. They found that the effect of prepared HAP is very close to natural HAP on the osteoblast cells. The decrease in size of HAP was improving cell proliferation and inhibited cell apoptosis [30]. Therefore, the morphology is correlated with the biological response of cells towards the implant. M.R. Nikpour et al. synthesized HAP and combined it with chitosan (CTS) and they found improvements in mechanical properties. The compressive strength reached around 14.47 ± 1.96 MPa in addition to the compressive modulus which reached 1470 ± 162 MPa [31]. Graphene oxide (GO) is a one atomic plane material consisting of carbon with a perfect two-dimensional structure [32]. Graphene compounds in general show extraordinary properties such as a huge Young's modulus reaching 1 TPa and tensile strength with a value around 130 GPa [33]. In addition, room temperature electrons mobility and consequently a good conductivity [34-36]. Further, good thermal conductivity, optical properties, and a large specific surface area [37]. Those interesting properties were confirmed and verified by many articles and researchers. GO is a special form of graphene (G) by the attachment of oxygen-containing groups on its surface including epoxy, hydroxyl, carboxylic, and carbonyl groups [38]. Therefore, biological properties as good biocompatibility, protecting DNA from the cleavage by enzymes, and nucleotide adsorption selectively [39]. Further, those functional groups turn the structure into an insulator material [40]. S. Pathmanapan et al. synthesized NCs of fibrin hydrogel and GO and they reported that cell viability exceeded 100% towards MG-63 cells due to the high biocompatibility of GO [41]. In

addition, J. Zhang et al. prepared NCs to contain cadmium oxide, polyalanine chitosan reduced graphene oxide, cobalt oxide, and silver oxide. The NC showed effective antibacterial properties, where the zone of inhibition against Escherichia coli (E. coli) was around 22.4 ± 0.0 mm, while 27.2 ± 0.03 mm against Staphylococcus aureus (S. aureus) [42]. Moreover, T. For et al. prepared NCs to contain GO and polyethersulfone and they found an improvement in the mechanical properties. The Young's modulus enhanced up to 1.95 ± 0.13 GPa, the tensile strength recorded 55.73 ± 15.21 MPa which can be considered relatively high values [43]. The route for the production of graphite and graphene oxide from Hassawi rice biomass waste produced in Eastern Saudi Arabia was illustrated at Scheme 1 .

Gadolinium oxide (Gd_2O_3) has been used in magnetic probes and optical applications, Gd(III) shows seven unpaired electrons and consequently a strong paramagnet. Therefore, it is used in magnetic resonance imagining [44, 45]. Gd_2O_3 also is a rare earth oxide with relatively high thermal and chemical stability and shows a large bandgap around 5.4 eV [46]. Besides, Gd_2O_3 shows good biocompatibility and therefore it is used in cell imaging. W. Yanli et al. prepared a nanocomposite of Eu^{3+}:Gd_2O_3 and the cell viability reached around 93% towards rat kidney cells [44]. Further, A. Wozniak et al. synthesized core-shell NCs of ZnO and Gd_2O_3 and after 2 days of incubation towards embryos for investigating the survival rate. They reported that the survival rate reached around 95% [47]. Therefore, fabricating NCs containing Gd_2O_3 and GO might enhance the optical and magnetic properties of HAP in addition to the biocompatibility, antibacterial activity and mechanical properties.

The current work is supposed to design nanocomposites with different combinations as binary/ternary NCs. The nanocomposites contain HAP, Gd_2O_3, and GO. TNC will have a hybrid matrix containing HAP/ Gd_2O_3 and reinforced with nanosheets of GO. The hybrid matrixes are hypothesized to directly affect the topology of the surface and the ratio between the two ingredients is adjusted at 1:1 in the composite. Therefore, the properties of HAP and Gd_2O_3 could be shown clearly. Further, the quantity of GO is much less than the other components to be a reinforcement material and to enhance the antibacterial and mechanical properties. In summary, this work is supposed to investigate and design ternary nanocomposites based on HAP/GO. Moreover, structural and physiochemical, and morphological studies will be done. The TNC will be tested in vitro towards different bacterial species and osteoblast cells.

2. Materials and methods

2.1. Inorganic chemicals

All purchased chemicals are calcium chloride dyhadrate ($CaCl_2.2H_2O$) (99%), ammonium (98%), gadolnium oxide (Gd_2O_3 (99%)), hydrochloric acid]hydrogen phosphate [$(NH_4)_2HPO_4$ (HCl, 33 %), potassium permenganet ($KMnO_4$, 98 %), graphite (98 %), ammonia solution (33 %). In addition, they were obtained from LOBA, ODISHA, and India.

2.2. Synthesis procedure

The preparation of HAP was done using co-precipitation with $CaCl_2$ **.**$2H_2O$ and with 0.5 M and 0.3 M respectively in separated beakers. The used water in all][$(NH_4)_2HPO_4$ stages was deionized water (DIW). The beakers are filled with 100 ml of DIW then the phosphate solution (P) is added slowly into the calcium one (Ca) and pH was kept at 11 ± 0.1 using NH_3. Then the mixture was stirred at 1200 rpm for 2 hours. Then the mixture is left for 1 day to be precipitated and the precipitated gel was washed and filtered several times then dried in a drying furnace 50 ^oC- 60 ^oC and the powder was collected. Graphite was produced from a natural source, Hassawi rice biomass waste from Al-Ahsa governorate at eastern Saudi Arabia region, according to the highlighted pathway in scheme 1.

GO is prepared using the modified hummers method [48]. By strong mixing of 0.5 g of graphite (G) added into 120 ml of H_2SO_4. Then 12 g of $KMnO_4$ was added into the mixture and stirred for 2 h. then it was followed by adding 300 ml of DIW with a slow rate (10 ml/h) then the mixture was cooled and slowly dropped with 10 ml of H_2O_2. Then the mixture was stirred for another 30 min at a high rate. The mixture was filtered then dispersed in 500 ml of HCL 20 wt% in ultrasonic for 15 min. finally, the mixture was dried at a temperature around 50 ^oC - 60 ^oC and collected.

All components were prepared, then the NCs were fabricated as followed: (1) 1 g of HAP, (2) 1 g of Gd_2O_3, (3) 1 g of HAP/ 1 g of Gd_2O_3, (4) 1 g of HAP/ 0.05 g GO, and (5) 1 g of HAP/1 g of Gd_2O_3 /0.05 g of GO.

The NCs were dispersed in five tubes separately, and all tubes contained 10 ml of DIW by ultrasonicator for 15 min. Then all the tubes were centrifuged for 10 min at 6000 rpm for collecting the powder samples. The obtained powders were dried for several hours at 50-60 ^{o}C.

2.3. XRD analysis

The structural analysis was done using (Pertpro, Cu $k_{\alpha 1}$ radiation, λ=1.5404 Å, 45 kV, 40 mA, Netherlands). Then the analysis of the patterns was done using Qualx software in addition to originlab software to plot the estimated patterns. The investigation was done in the range of 5^{o}-60^{o}.

2.4. FTIR measurements

The spectrum of FTIR was estimated using a spectrometer of (Perkin-Elmer 2000) for all compositions in the range of 400-4000 cm^{-1}.

2.5. XPS measurements

The final powder was investigated using (PerkinElmer PHI 5600) XPS instrument up to 1400 eV and with 0.1 eV resolution.

2.6. TEM

The transmission electron microscopy (TEM, JEOL/JME 2100) was used to investigate the morphology and microstructure of the nanocomposite.

2.7. FESEM

A field emission scanning electron microscope (FESEM, model: QUANTA-FEG250, Netherlands) was used for investigating the surface morphology and topology of NCs by analyzing the micrographs with Gwyddion 2.4 software. Further, the dimension analysis was done and measured by Image J 1.53e software. The elemental analysis has been done via the Energy-dispersive X-ray spectroscopy (EDX), which is set up with FESEM apparatus.

2.8. BET

(Nova 2000 series – Quantachrome-USA) was used to get the surface area data. The samples were dried at 60 ^{o}C.

2.9. In vitro cell viability tests

In Dulbecco's modified Eagle's medium (DMEM, Gibpco) with 5% CO_2 and at 37 ^{o}C, the human osteoblastic cell line was cultured for measuring the ratio of cell viability.

By putting 5 mg/20 ml of all samples in a 96 well plate and they were sterilized. The cell density towards all samples was constant, around 5×10^3 cells/cm^2. The system was incubated for 3 days, the medium was removed, then was injected with MTT. Then by an optical analyzer, the viability ratio was detected and calculated as [49]:

$$\text{Viability } (\%) = \frac{\text{Optical density of samples}}{\text{Optical density of control}} \times 100$$

The standard deviation and statistical analysis were estimated using Medcalc 15.0 software with repeating the experiment three times.

2.10. Antibacterial activity

The anti-bacterial behavior was measured by using the diffusion desk method. 20 mg/ml of powder was taken to be measured from all compositions. Then the zone of inhibition was recorded to indicate the antibacterial behavior after 24 h of exposure. The exposure was against Staphylococcus aureus was obtained (S.aureus), which was obtained from American Type Culture Collection (ATCC) Number 29213, while Escherichia coli was obtained (*E. coli*) from ATCC number 25922. The experiment was repeated three times to obtain the standard deviation.

2.11. Microhardness study

The microhardness was studied using (TTS UNLIMITED INC. model: HWDM-7/Japan) with the imaging mode.

3. Results and discussions

3.1. XRD

The patterns of all compositions are plotted in Fig. 1 and the hexagonal structure of HAP is found from its most obvious peaks at 31.86° and 25.91°. These peaks belong to the (hkl) planes of (211) and (002). Further, the lattice parameters a and c are calculated with the value of 9.4285 and 6.7476 Å, respectively. Furthermore, the volume of the hexagonal cell is around 519.476 $Å^3$ which matches with the value of ICDD no. 01-073-0293. The peaks of HAP are broad which indicates the low crystallinity of HAP and the formation of small crystals. Moreover, Gd_2O_3 is detected as a cubic phase according to ICDD no. 00-210-6881 with its characteristic peaks at 28.39°, 33 °, 47.49 °, and 56.28°. The detected peaks refer to the planes of (222), (400),(440), and (622), respectively. The calculated lattice constant a and volume are around 10.844 Å and 1275.2 $Å^3$. The peaks of Gd_2O_3 are sharper than HAP which refers to the relatively high crystallinity.

3.2. FTIR

The FTIR spectra are shown in Fig. 2 and the values of transmittance bands are reported in Table 1. The HAP phase can be seen with the existence of bands containing different modes of P-O such as 477,568, 605, and 1096 cm^{-1} which refer to vibrational, bending, and stretching modes of O-P-O [50]. Further, the noticed bands at 413, 965, and 1035 cm^{-1} might belong to bending and stretching modes of PO_4^{3-} [51]. The affinity of HAP to absorb carbon dioxide during the preparation stage can be noticed by the existence of CO_3^{2-} vibrational modes at 1421 cm^{-1} [52].

Table 1. The bands of FTIR analysis and their assignments.

HAP	Gd_2O_3	HAP/ Gd_2O_3	HAP/GO	HAP/ Gd_2O_3 /GO	Assignment	Ref.
---	410	405	---	---	Gd-O	[53]
413	---	---	---	---	bending mode of PO_4^{3-}	[51]
477	---	---	473	---	vibrational mode of O-P-O	[54]
568	---	565	565	566	bending mode of O-P-O	[55]
605	---	604.6	603.6	603.6	bending mode of O-P-O	[56]
878	---	873	875	874	vibrational mode of CO_3^{2-}	[52]

965	---	---	964	963	PO_4^{3-}stretching	[57]
1035	---	1034	1033	1032	anti-symetric stretch of PO_4^{3-}	[58]
1096	---	---	1092	1093.4	P-O stretching	[50]
1421	---	1419	1423	1417	vibrational mode of CO_3^{2-}	[59]
1463	---	---	1457	1489	C-O	[57, 59]
1640	1631	1638	1644	1631	absorbed water	[57]
2922	2920	2918	2922	2920	C-H vibrations	[52, 59]
3439	3435	3436	343438	3414	O-H vibrations	[60]

3.3.XPS

The detected peaks by the XPS are illustrated in Fig. 3(a-f) and listed in Table 2. The existence of O is detected at 532.28 eV which belongs to 1s orbital in addition to O-C=O and C-O which are at 531.88 and 531.64 eV respectively [61]. Further, P is found by examining 2p orbital at 134.27 eV and using the high-resolution examination, $P2p_{1/2}$ is detected at 133.64 eV [62]. Furthermore, Ca is detected in the survey at 348.41 eV at the state of orbital $2p_{1/2}$ and $2p_{3/2}$ at The formation of GO can be confirmed by confirming O existence 351.12 and 347.58 eV [63]. and C 1s, where at 285.16, 288.54, and 289.55 eV peaks which belong to C-O, C=C, and O-C=O respectively, and these groups are formed on the surface of GO [64]. Moreover, Gd 4d is observed at 144.79 eV, while Gd 3d is found at 1189.42 eV [65].

Table 2. The results of XPS investigation upon TNC of HAP/Gd_2O_3/GO.

Band	Binding energy (eV)	Assignment	Refrence
O 1s	531.88	O-C=O	[61]
O 1s	531.64	C-O	[61]
P 2p	133.64	$P2p_{1/2}$	[62]
C 1s	285.16	C-O	[63]
C 1s	288.54	C=C	[64]
C 1s	289.55	O-C=O	[64]

Ca 2p	347.58	$Ca2p_{3/2}$	[62]
Ca 2p	351.12	$Ca2p_{1/2}$	[62]
Gd 4d	144.79	Gd	[63]

3.4. TEM

The TEM technique is used to investigate the shape and size of NCs which clarify microstructural changes to be connected with the chemical and structural studies to deeply understand the biological response. All images are demonstrated in Fig. 4(a-d) for HAP, Gd_2O_3 in addition to NC of their combination and TNC. It can be noticed that HAP and Gd_2O_3 display rod shape particles, which makes them difficult to be distinguished. The pure HAP shows nanorods with average length and diameter around 37 and 10.5 nm respectively, while pure Gd_2O_3 shows larger dimensions around 40 and 12 nm respectively. The difference in size can be ascribed to the difference in crystallinity which is noticed as higher for Gd_2O_3 in XRD. Therefore, larger crystallites are formed and led to larger particles. However, the NC of HAP/Gd_2O_3 exhibits a wide range of sizes with an average diameter and length around 12 and 36 nm, respectively. Moreover, GO is noticed as a nanosheet with nanorods are grown on its surface. The TNC shows fewer aggregations which might indicate a less rough surface which can directly affect the amount of the releasing ions. Furthermore, the dimensions of nanorods are around 9.5 and 27 nm for diameter and length respectively. The incorporation of GO nano-sheets inside the matrix of nanorods can affect directly the mechanical properties by filling pores leading to inhibiting crack propagation [66]. Therefore, the maximum tensile strength and fracture can be enhanced.

3.5. Surface topography

The surface morphology is studied using FESEM and illustrated in Fig. 5(a-d). There are two obvious shapes which are nanorods and nanosheets with non-uniform size distribution. The pure HAP shows smaller nanorods than Gd_2O_3 which matches well with the results of TEM images. The diameter and length of HAP are around 24 and 87 nm, while around 35 and 98 nm for Gd_2O_3/HAP. The topology of HAP seems to be rough and that might be due to its low crystallinity. In general, the nano-sized materials contain a high surface area, and more grain boundaries leading to more reactivity at these boundaries [67]. Therefore, the high density of

crystallographic defects directly affects biological performance by improving the number of active sites [68]. On the other hand, NC of HAP/Gd_2O_3 shows large grains for Gd_2O_3 and small ones for HAP which might increase the smoothness of the composition and increase the average size in addition to relatively high porosity. The increase in porosity induces a larger channel to nutrient and oxygen transportations into the cells [69]. Further, NC which contains GO and HAP shows nanorods aggregations on the nanosheet surface of GO with a diameter around 20 nm and length around 80 nm. This means a decrease in the size of HAP grains which can be ascribed to the ability of GO to inhibit the growth of nanorods. Furthermore, TNC shows nanorods and nanosheets with relatively lower porosity which can affect the biological response. The diameter and length of nanorods increased to be around 25 and 85 nm respectively. However, the incorporation of nanosheets into the nanorod matrix in the existence of a relatively high porosity can affect directly on the mechanical properties and biological response and cell adhesion between the biomaterial and osteoblast cells.

3.6 Roughness behavior

The topographical investigation of all compositions based on FESEM micrographs and all graphs is demonstrated in Fig. 6(a-d), while the numerical results are listed in Table 3. The highest roughness average (R_a) belongs to HAP and NC of HAP/GO with the same value of 4.8 nm. The difference lies in the other parameters where, the maximum height of roughness (R_t) for HAP is around 41.6 nm, while for HAP/GO is around 55.7 nm. In addition, other important parameters must be taken into consideration as skewness (R_{sk}) and kurtosis (R_{ku}) which are 0.1 and 3.6 nm for HAP, while -0.3 and 5.9 nm for HAP/GO. That can indicate that at HAP/GO despite high roughness which means high surface area and more available sites, the viable cells will not increase dramatically. The negative value of R_{sk} in HAP/GO refers to the tendency of the material to form valleys more than asperities, while the relatively high value of R_{ku} indicates that the peaks in that sample are sharper than the others [70]. Therefore, a sharp valley can induce relatively low-stress concentration than sharp asperities which can affect stresses lied on the cells from the implant [71]. However, the R_a at TNC decreased to 4.1 and the sharpness increased in the value of forming asperities, where R_{sk} and R_{ku} are around 0.3 and 3.7 nm respectively. The decrease in R_a at TNC can indicate a decrease in the contact area and consequently might improve the lifetime of the implant lowering the released ions [72].

Table 3. The roughness parameters for all compositions.

composition	R_a (nm)	R_q (nm)	R_t (nm)	R_v (nm)	R_p (nm)	R_{tm} (nm)	R_{sk}	R_{ku}
HAP	4.8	6.3	41.6	20.1	21.5	33.6	0.1	3.6
HAP/Gd_2O_3	4.1	5.5	41.1	20.1	21	28.8	-0.2	4.5
HAP/GO	4.8	7.0	55.7	27.9	27.8	32.6	-0.3	5.9
HAP/GO/Gd_2O_3	4.1	5.4	36.1	15.2	20.8	26.7	0.3	3.7

3.7. EDX

The elemental analysis EDX can confirm the existence of compounds on the surface based on FESEM which can give an indication about the stoichiometric value of the components. However, the results are listed in Table 4 and illustrated in Fig. 7. The oxygen shows a 50.15% atomic percentage due to its existence in all compounds. Further, the Ca/P ratio is around 1.4 which is close to the stoichiometric ratio of 1.67. In addition, detecting carbon with 18.71% atomic percent can confirm the existence of a carbon compound which is GO. The detection of all elements can confirm the formation of TNC of HAP/ Gd_2O_3/GO.

Table 4. The elements of TNC from EDX analysis with their percentages.

Element	Atomic %	Weight %
C K	18.71	9.83
O K	50.15	35.1
P K	12.51	16.96
GdL	1.06	7.31
CaK	17.56	30.79

3.8. BET

The adsorption-desorption hysteresis is plotted in Fig 8 between the relative pressure and the volume adsorbed by nitrogen gas while Table 5 shows the calculated values. The cumulative

surface area of HAP/Gd_2O_3 is around 47.04 m^2/g which is higher than the same surface area using DFT method of TNC which is around 44.62 m^2/g. That result was predictable and noticed in the topological analysis in the roughness section. The surface of HAP/ Gd_2O_3 was rougher than TNC which explains why the surface area of TNC is smaller. In addition, the total average particle radius using BET was higher for TNC. On the other hand, BET calculated the average of all particles. However, the total average pore size of HAP/ Gd_2O_3 is larger than HAP/ Gd_2O_3/GO which can affect directly on the biological response. The more porosity and pore size or volume, the more nutrients and oxygen can be reached to the cells [73]. Therefore, more proliferation and more viable cells.

Table 5. The numerical values of Barrett-Joyner-Halenda (BJH) analysis of HAP/ Gd_2O_3 and TNC of HAP/ Gd_2O_3/GO.

Property	HAP/Gd_2O_3	HAP/Gd_2O_3/GO
DFT method cumulative surface area	47.04 (m^2/g)	44.62 (m^2/g)
DR method micropore surface area	160.66 (m^2/g)	114.08 (m^2/g)
Total Pore Volume	0.184 cm^3/g	0.169 cm^3/g
Average Pore Size	7.99 nm	7.72 nm
BET Surface area	46.07 m^2/g	43.81 m^2/g
Average Particle radius	29.25 nm	31.12 nm

3.9. Antibacterial activity

The combination of HAP, Gd_2O_3, and GO shows an improvement in the activity against both strains. The graph is plotted in Fig. 9 in addition to a comparison between different combinations and their results. Pure HAP showed no activity against both strains, while Gd_2O_3 exhibited a zone of inhibition around 13.4 ± 0.4 and 13.8 ± 0.2 mm against E. coli and S. aureus respectively. The addition of Gd_2O_3 into the HAP matrix showed a zone of inhibition around 12.5 ± 0.3 and 12.9 ± 0.4 mm against both strains. Further, GO with no addition showed antibacterial behavior reached 13.2 ± 0.5 and 13.8 ± 0.3 mm, while the TNC showed enhancement in that

behavior which reached 14.6 ± 0.4 and 15.2 ± 0.4 mm against E. coli and S. aureus, respectively as in Table 6. The enhancement of antibacterial activity can be ascribed to the existence of GO and Gd_2O_3 which have shown antibacterial behavior in their pure phases. Furthermore, the morphology of GO which showed as sheets can indicate more sharp edges which can cause damage to the bacterial cell membrane [74, 75]. Moreover, the nanoparticles can penetrate the bacterial cells and directly harm DNA or essential components in bacteria in addition to the reactive oxygen species (ROS) which might be formed [76, 77].

Table 6. A comparison between different nanocomposites according to the antibacterial activities.

Composition	Inhibition zone of E. coli (mm)	Inhibition zone of S.aureus (mm)	Reference
Ag-HAP	18 ± 0.5	17 ± 0.5	[78]
HAP/PCL/gentamicin	~4.2	--	[79]
HAP/Ag	19	21	[80]
CTS/PVA	4	6.3	[81]
CTS/PVA/GO/HAP/Au	17	18	[81]
HAP/GO/CdSe	20.4	21.4	[82]
HAP/GO/Ag/cellulose	--	25	[83]
HAP/Cs/PVA/Au	13	15	[81]
Gentamicin sulfate/HAP/phosphate glass	32.9 ± 0.1	31 ± 0.4	[84]
ZnO/HAP	11 ± 0.3	16 ± 0.3	[85]
HAP/GO/ Gd_2O_3	14.6 ± 0.4	13.8 ± 0.3	Current study

3.10. Cell viability

The cytotoxicity of all compositions towards osteoblast human cell line is illustrated in Fig. 10. The non-toxic effect of HAP can be noticed where the viable cells are around 95.6 ± 0.6 % of the control sample. Also, Gd_2O_3 showed good biocompatibility with a value of 94.3 ± 0.7 % and therefore the NC of HAP/ Gd_2O_3 showed 94.8 ± 0.9 % which can be considered as low

cytotoxicity. Further, HAP/GO showed 95.2 ± 0.6 % which indicates the non-toxic effect of GO. Therefore, HAP/Gd_2O_3/GO exhibited cell viability around 96.7 ± 0.5 % which is an improvement in the number of viable cells due to the existence of three biocompatible components in one composite. The small number of released ions in the NCs led to high cell viability in addition to the existence of Ca^{2+} and P^{5+} ions from the HAP structure which can increase the adhesion and an essential for growing the cells. Moreover, the enhancement in morphology and size of particles might affect by increasing the adhesion of the cells with the composite.

3.11. Microhardness

The microhardness is an indication of the mechanical properties and that refers to the ability of the material to resist the penetration. The pure HAP shows microhardness around 2.8 ± 0.1 GPa, while the pure Gd_2O_3 shows less resistance with a value of 2.4 ± 0.2 GPa. The addition of Gd_2O_3 to HAP can aim to enhance the mechanical properties of Gd_2O_3 and hardness reached 2.7 ± 0.2 for the NC. The NC of HAP/GO showed microhardness around 2.8 ± 0.1 GPa, while TNC of HAP/ Gd_2O_3/GO exhibited development in the resistance of penetration, where hardness reached 3.1 ± 0.2 Gpa which is close to the previous results as seen in Table 7. The enhancement of mechanical properties can be ascribed to the ability of GO to inhibit the crack propagation inside the HAP matrix. In addition, The sheet structure of GO might fill the pores which reinforced the composite [86, 87]. The improvement in mechanical properties can introduce enough support for the growing tissues.

Table 7. A comparison between different composites containing HAP.

Composition	Microhardness (GPa)	Reference
HAP/multi-walled carbon nanotubes	4.0	[88]
TiO_2/HAP	0.13	[89]
Co/Cr/Mo alloy	3.7	[90]
Co/Cr/Mo/HAP	5.7	[90]
Polyetheretherketone/HAP	0.3	[91]
Silk fibron/HAP	~0.4	[92]
HAP/GO/ Gd_2O_3	3.1 ± 0.2	Current study

4. Conclusion

Hydroxyapatite (HAP) was synthesized via chemical co-precipitation and then it was combined with graphene oxide (GO) and gadolinium oxide (Gd_2O_3) to form a ternary nanocomposite (TNC). The average roughness parameter (R_a) decreased from 4.8 to 4.1 nm, while R_{sk} and R_{ku} parameters increased from 0.1 and 3.6 nm to 0.3 and 3.7 nm respectively. Furthermore, the morphological examination showed that Gd_2O_3 and HAP were with the same shape which is nanorod shape. The diameter of nanorods decreased from 10.5 to 9.5 nm, while the length started at 37 nm and decreased to 27 nm. Moreover, the total pore volume decreased from 0.184 to 0.169 cm^3/g. In addition, BET surface area started from 46.07 to 43.81 m^2/g from NC of HAP/ Gd_2O_3 to HAP/ Gd_2O_3/GO respectively. The mechanical properties enhanced, where hardness improved from 2.8 ± 0.1 to 3.1 ± 0.2 GPa from pure HAP to TNC. Furthermore, in vitro study shows that antibacterial activity of poor HAP developed by the addition of GO and Gd_2O_3 and reached 14.6 ± 0.4 and 15.2 ± 0.4 against E. coli and S. aureus respectively.

Conflicts of interest

The authors declare that they have no conflict of interest.

References

1. Souza, E. Q. M., Klaus, A. E. C., Santos, B. F. E., da Costa, M. C., Ervolino, E., de Lima, D. C., & Fernandes, L. A. (2020). Evaluations of hydroxyapatite and bioactive glass in the repair of critical size bone defects in rat calvaria. *Journal of Oral Biology and Craniofacial Research*, *10*(4), 422-429.
2. Roddy, E., DeBaun, M. R., Daoud-Gray, A., Yang, Y. P., & Gardner, M. J. (2018). Treatment of critical-sized bone defects: clinical and tissue engineering perspectives. *European Journal of Orthopaedic Surgery & Traumatology*, *28*(3), 351-362.
3. Zhang, M., Matinlinna, J. P., Tsoi, J. K., Liu, W., Cui, X., Lu, W. W., & Pan, H. (2020). Recent developments in biomaterials for long-bone segmental defect reconstruction: A narrative overview. *Journal of Orthopaedic Translation*, *22*, 26-33.
4. Bal, Z., Kaito, T., Korkusuz, F., & Yoshikawa, H. (2020). Bone regeneration with hydroxyapatite-based biomaterials. *Emergent Materials*, *3*(4), 521-544.

5. Tang, X. Z., Kumar, P., Alavi, S., & Sandeep, K. P. (2012). Recent advances in biopolymers and biopolymer-based nanocomposites for food packaging materials. *Critical reviews in food science and nutrition*, *52*(5), 426-442.
6. Gao, M., Liu, B., Zhang, X., Zhang, Y., Li, X., & Han, G. (2022). Ultrathin MoS_2 nanosheets anchored on carbon nanofibers as free-standing flexible anode with stable lithium storage performance. *Journal of Alloys and Compounds*, *894*, 162550.
7. Liu, H., Li, X., Ma, Z., Sun, M., Li, M., Zhang, Z., ... & Guo, S. (2021). Atomically Dispersed Cu Catalyst for Efficient Chemoselective Hydrogenation Reaction. *Nano Letters*, *21*(24), 10284-10291.
8. Liu, W., Zheng, Y., Wang, Z., Wang, Z., Yang, J., Chen, M., ... & Wei, L. (2021). Ultrasensitive Exhaled Breath Sensors Based on Anti-Resonant Hollow Core Fiber with In Situ Grown ZnO-Bi_2O_3 Nanosheets. *Advanced Materials Interfaces*, *8*(6), 2001978.
9. Li, G., Yuan, H., Mou, J., Dai, E., Zhang, H., Li, Z., ... & Zhang, X. (2021). Electrochemical detection of nitrate with carbon nanofibers and copper co-modified carbon fiber electrodes. *Composites Communications*, 101043.
10. Mu, S., Liu, Q., Kidkhunthod, P., Zhou, X., Wang, W., & Tang, Y. (2021). Molecular grafting towards high-fraction active nanodots implanted in N-doped carbon for sodium dual-ion batteries. *National science review*, *8*(7), nwaa178.
11. Wang, M., Mi, G., Shi, D., Bassous, N., Hickey, D., & Webster, T. J. (2018). Nanotechnology and nanomaterials for improving neural interfaces. *Advanced Functional Materials*, *28*(12), 1700905.
12. McMahon, R. E., Wang, L., Skoracki, R., & Mathur, A. B. (2013). Development of nanomaterials for bone repair and regeneration. *Journal of Biomedical Materials Research Part B: Applied Biomaterials*, *101*(2), 387-397.
13. Xiong, Q. M., Chen, Z., Huang, J. T., Zhang, M., Song, H., Hou, X. F., ... & Feng, Z. J. (2020). Preparation, structure and mechanical properties of Sialon ceramics by transition metal-catalyzed nitriding reaction. *Rare Metals*, *39*(5), 589-596.
14. Molla, M. A. I., Furukawa, M., Tateishi, I., Katsumata, H., Suzuki, T., & Kaneco, S. (2018). Photocatalytic degradation of fenitrothion in water with TiO_2 under solar irradiation. *Water Conservation & Management (WCM)*, *2*(2), 1-5.

15. Jia, J. S., Cao, Y., Wu, T. X., Tao, Y., Pan, Y. M., Huang, F. P., & Tang, H. T. (2021). Highly Regio-and Stereoselective Markovnikov Hydrosilylation of Alkynes Catalyzed by High-Nuclearity {Co14} Clusters. *ACS Catalysis*, *11*(12), 6944-6950.
16. Zhang, J., Zhao, Y., Liu, Y., Zhu, C., Wang, B., Zhang, L., ... & Zhang, X. (2022). Pd/PANI/Ti Composite Electrocatalyst with Efficient Electrocatalytic Performance: Synthesis, Characterization, Stability, Kinetic Studies, and Degradation Mechanism. *Journal of Alloys and Compounds*, 163723.
17. Zhang, X., Tang, Y., Zhang, F., & Lee, C. S. (2016). A novel aluminum–graphite dual-ion battery. *Advanced energy materials*, *6*(11), 1502588.
18. Wang, G., Liu, D., Fan, S., Li, Z., & Su, J. (2021). High-k erbium oxide film prepared by sol-gel method for low-voltage thin-film transistor. *Nanotechnology*, *32*(21), 215202.
19. Yan, W., Cao, M., Fan, S., Liu, X., Liu, T., Li, H., & Su, J. (2021). Multi-yolk $ZnSe_2$ ($CoSe_2$)@ NC heterostructures confined in N-doped carbon shell for high-efficient sodium-ion storage. *Composites Part B: Engineering*, *213*, 108732.
20. Zhu, H., Zhu, J., Zhang, Z., & Zhao, R. (2021). Crossover from linear chains to a honeycomb network for the nucleation of hexagonal boron nitride grown on the Ni (111) surface. *The Journal of Physical Chemistry C*, *125*(48), 26542-26551.
21. Du, X., Tian, W., Pan, J., Hui, B., Sun, J., Zhang, K., & Xia, Y. (2022). Piezo-phototronic effect promoted carrier separation in coaxial pn junctions for self-powered photodetector. *Nano Energy*, *92*, 106694.
22. Wang, M., Jiang, C., Zhang, S., Song, X., Tang, Y., & Cheng, H. M. (2018). Reversible calcium alloying enables a practical room-temperature rechargeable calcium-ion battery with a high discharge voltage. *Nature chemistry*, *10*(6), 667-672.
23. Gupta, J. K., & Gupta, S. K. (2018). A Comparative Study of Crowd Counting and Profiling Through Visual and Non-Visual Sensors. *Recent Trends in Science, Technology, Management and Social Development*, 89.
24. Satrio Yudho (2020). Construction of Lora Data Power Sensor from Giot and Acsip Using Sql Technique. Acta Electronica Malaysia, 4(2): 51-55.
25. Tang, X., Wu, J., Wu, W., Zhang, Z., Zhang, W., Zhang, Q., ... & Li, P. (2020). Competitive-type pressure-dependent immunosensor for highly sensitive detection of diacetoxyscirpenol in wheat via monoclonal antibody. *Analytical chemistry*, *92*(5), 3563-3571.

26. Nayak, A. K. (2010). Hydroxyapatite synthesis methodologies: an overview. *International Journal of ChemTech Research*, *2*(2), 903-907.
27. Ma, G. (2019, November). Three common preparation methods of hydroxyapatite. In *IOP Conference Series: Materials Science and Engineering* (Vol. 688, No. 3, p. 033057). IOP Publishing.
28. Sáenz, A., Rivera, E., Brostow, W., & Castaño, V. M. (1999). Ceramic biomaterials: an introductory overview. *Journal of Materials Education*, *21*(5/6), 267-276.
29. Halim, N. A. A., Hussein, M. Z., & Kandar, M. K. (2021). Nanomaterials-upconverted hydroxyapatite for bone tissue engineering and a platform for drug delivery. *International journal of nanomedicine*, *16*, 6477.
30. Shi, Z., Huang, X., Cai, Y., Tang, R., & Yang, D. (2009). Size effect of hydroxyapatite nanoparticles on proliferation and apoptosis of osteoblast-like cells. *Acta biomaterialia*, *5*(1), 338-345.
31. Nikpour, M. R., Rabiee, S. M., & Jahanshahi, M. J. C. P. B. E. (2012). Synthesis and characterization of hydroxyapatite/chitosan nanocomposite materials for medical engineering applications. *Composites Part B: Engineering*, *43*(4), 1881-1886.
32. Sun, L. (2019). Structure and synthesis of graphene oxide. *Chinese Journal of Chemical Engineering*, *27*(10), 2251-2260.
33. Gupta, K. K., Mukhopadhyay, T., Roy, A., & Dey, S. (2020). Probing the compound effect of spatially varying intrinsic defects and doping on mechanical properties of hybrid graphene monolayers. *Journal of Materials Science & Technology*, *50*, 44-58.
34. Wu, Z. S., Ren, W., Gao, L., Zhao, J., Chen, Z., Liu, B., ... & Cheng, H. M. (2009). Synthesis of graphene sheets with high electrical conductivity and good thermal stability by hydrogen arc discharge exfoliation. *ACS nano*, *3*(2), 411-417.
35. Mohanraj, J., Durgalakshmi, D., Rakkesh, R. A., Balakumar, S., Rajendran, S., & Karimi-Maleh, H. (2020). Facile synthesis of paper based graphene electrodes for point of care devices: A double stranded DNA (dsDNA) biosensor. *Journal of Colloid and Interface Science*, *566*, 463-472.
36. Tahernejad-Javazmi, F., Shabani-Nooshabadi, M., & Karimi-Maleh, H. (2019). 3D reduced graphene oxide/$FeNi_3$-ionic liquid nanocomposite modified sensor; an electrical synergic

effect for development of tert-butylhydroquinone and folic acid sensor. *Composites Part B: Engineering*, *172*, 666-670.

37. Mohammed, H., Kumar, A., Bekyarova, E., Al-Hadeethi, Y., Zhang, X., Chen, M., ... & Rimondini, L. (2020). Antimicrobial mechanisms and effectiveness of graphene and graphene-functionalized biomaterials. A scope review. *Frontiers in Bioengineering and Biotechnology*, *8*, 465.
38. Wright, Z. M., Arnold, A. M., Holt, B. D., Eckhart, K. E., & Sydlik, S. A. (2019). Functional graphenic materials, graphene oxide, and graphene as scaffolds for bone regeneration. *Regenerative Engineering and Translational Medicine*, *5*(2), 190-209.
39. Wu, S. Y., An, S. S. A., & Hulme, J. (2015). Current applications of graphene oxide in nanomedicine. *International journal of nanomedicine*, *10*(Spec Iss), 9.
40. Thompson, B. C., Murray, E., & Wallace, G. G. (2015). Graphite oxide to graphene. Biomaterials to bionics. *Advanced Materials*, *27*(46), 7563-7582.
41. Pathmanapan, S., Periyathambi, P., & Anandasadagopan, S. K. (2020). Fibrin hydrogel incorporated with graphene oxide functionalized nanocomposite scaffolds for bone repair—In vitro and in vivo study. *Nanomedicine: Nanotechnology, Biology and Medicine*, *29*, 102251.
42. Zhang, J., Ding, E., Xu, S., Li, Z., Fakhri, A., & Gupta, V. K. (2020). Production of metal oxides nanoparticles based on poly-alanine/chitosan/reduced graphene oxide for photocatalysis degradation, anti-pathogenic bacterial and antioxidant studies. *International Journal of Biological Macromolecules*, *164*, 1584-1591.
43. Forati, T., Atai, M., Rashidi, A. M., Imani, M., & Behnamghader, A. (2014). Physical and mechanical properties of graphene oxide/polyethersulfone nanocomposites. *Polymers for advanced technologies*, *25*(3), 322-328.
44. Li, I. F., Su, C. H., Sheu, H. S., Chiu, H. C., Lo, Y. W., Lin, W. T., ... & Yeh, C. S. (2008). $Gd_2O(CO_3)_2 \cdot H_2O$ particles and the corresponding Gd_2O_3: synthesis and applications of magnetic resonance contrast agents and template particles for hollow spheres and hybrid composites. *Advanced Functional Materials*, *18*(5), 766-776.
45. Rahman, A. A., Vasilev, K., & Majewski, P. (2011). Ultra small Gd_2O_3 nanoparticles: Absorption and emission properties. *Journal of colloid and interface science*, *354*(2), 592-596.

46. Yanli, W. U., Xianzhu, X. U., Qianlan, L. I., Ruchun, Y. A. N. G., Haixin, D. I. N. G., & Qiang, X. I. A. O. (2015). Synthesis of bifunctional Gd_2O_3: Eu^{3+} nanocrystals and their applications in biomedical imaging. *Journal of Rare Earths*, *33*(5), 529-534.
47. Woźniak, A., Grześkowiak, B. F., Babayevska, N., Zalewski, T., Drobna, M., Woźniak-Budych, M., ... & Jurga, S. (2017). ZnO@ Gd_2O_3 core/shell nanoparticles for biomedical applications: Physicochemical, in vitro and in vivo characterization. *Materials Science and Engineering: C*, *80*, 603-615.
48. Ahmed, M. K., El-Naggar, M. E., Aldalbahi, A., El-Newehy, M. H., & Menazea, A. A. (2020). Methylene blue degradation under visible light of metallic nanoparticles scattered into graphene oxide using laser ablation technique in aqueous solutions. *Journal of Molecular Liquids*, *315*, 113794.
49. Mansour, S. F., El-dek, S. I., Ismail, M., & Ahmed, M. K. (2018). Structure and cell viability of Pd substituted hydroxyapatite nano particles. *Biomedical Physics & Engineering Express*, *4*(4), 045008.
50. Lin, K., Zhou, Y., Zhou, Y., Qu, H., Chen, F., Zhu, Y., & Chang, J. (2011). Biomimetic hydroxyapatite porous microspheres with co-substituted essential trace elements: surfactant-free hydrothermal synthesis, enhanced degradation and drug release. *Journal of Materials Chemistry*, *21*(41), 16558-16565.
51. Lukić, M. J., Veselinović, L., Stevanović, M., Nunić, J., Dražič, G., Marković, S., & Uskoković, D. (2014). Hydroxyapatite nanopowders prepared in the presence of zirconium ions. *Materials Letters*, *122*, 296-300.
52. Ahmed, M. K., Ramadan, R., El-Dek, S. I., & Uskoković, V. (2019). Complex relationship between alumina and selenium-doped carbonated hydroxyapatite as the ceramic additives to electrospun polycaprolactone scaffolds for tissue engineering applications. *Journal of Alloys and Compounds*, *801*, 70-81.
53. Liu, G., Hong, G., & Sun, D. (2004). Synthesis and characterization of SiO_2/Gd_2O_3: Eu core–shell luminescent materials. *Journal of colloid and interface science*, *278*(1), 133-138.
54. Hiromoto, S., Inoue, M., Taguchi, T., Yamane, M., & Ohtsu, N. (2015). In vitro and in vivo biocompatibility and corrosion behaviour of a bioabsorbable magnesium alloy coated with octacalcium phosphate and hydroxyapatite. *Acta biomaterialia*, *11*, 520-530.

55. Kaygili, O., Tatar, C., Yakuphanoglu, F., & Keser, S. (2013). Nano-crystalline aluminum-containing hydroxyapatite based bioceramics: synthesis and characterization. *Journal of sol-gel science and technology*, *65*(2), 105-111.
56. Janković, A., Eraković, S., Mitrić, M., Matić, I. Z., Juranić, Z. D., Tsui, G. C., ... & Park, S. J. (2015). Bioactive hydroxyapatite/graphene composite coating and its corrosion stability in simulated body fluid. *Journal of Alloys and Compounds*, *624*, 148-157.
57. Kaygili, O., Keser, S., Bulut, N., & Ates, T. (2018). Characterization of Mg-containing hydroxyapatites synthesized by combustion method. *Physica B: Condensed Matter*, *537*, 63-67.
58. Gopi, D., Rajeswari, D., Ramya, S., Sekar, M., Pramod, R. D., Dwivedi, J., ... & Ramaseshan, R. (2013). Enhanced corrosion resistance of strontium hydroxyapatite coating on electron beam treated surgical grade stainless steel. *Applied surface science*, *286*, 83-90.
59. Mansour, S. F., El-Dek, S. I., & Ahmed, M. K. (2017). Physico-mechanical and morphological features of zirconia substituted hydroxyapatite nano crystals. *Scientific reports*, *7*(1), 1-21.
60. Mishra, V. K., Bhattacharjee, B. N., Parkash, O., Kumar, D., & Rai, S. B. (2014). Mg-doped hydroxyapatite nanoplates for biomedical applications: a surfactant assisted microwave synthesis and spectroscopic investigations. *Journal of alloys and compounds*, *614*, 283-288.
61. Donya, H., Darwesh, R., & Ahmed, M. K. (2021). Morphological features and mechanical properties of nanofibers scaffolds of polylactic acid modified with hydroxyapatite/CdSe for wound healing applications. *International Journal of Biological Macromolecules*, *186*, 897-908.
62. Zavala-Sanchez LA, Hirata GA, Novitskaya E, Karandikar K, Herrera M, Graeve OA. Distribution of Eu^{2+} and Eu^{3+} Ions in Hydroxyapatite: A Cathodoluminescence and Raman Study. ACS biomaterials science & engineering 2015;1:1306-13.
63. Negrila, C. C., Predoi, M. V., Iconaru, S. L., & Predoi, D. (2018). Development of zinc-doped hydroxyapatite by sol-gel method for medical applications. *Molecules*, *23*(11), 2986.
64. Wang, M., Liu, Y., Ren, G., Wang, W., Wu, S., & Shen, J. (2018). Bioinspired carbon quantum dots for sensitive fluorescent detection of vitamin B12 in cell system. *Analytica chimica acta*, *1032*, 154-162.
65. Chastain, J., & King Jr, R. C. (1992). Handbook of X-ray photoelectron spectroscopy. *Perkin-Elmer Corporation*, *40*, 221.

66. Li, M., Liu, Q., Jia, Z., Xu, X., Cheng, Y., Zheng, Y., ... & Wei, S. (2014). Graphene oxide/hydroxyapatite composite coatings fabricated by electrophoretic nanotechnology for biological applications. *Carbon*, *67*, 185-197.
67. Ramay, H. R., & Zhang, M. (2004). Biphasic calcium phosphate nanocomposite porous scaffolds for load-bearing bone tissue engineering. *Biomaterials*, *25*(21), 5171-5180.
68. Zou, S., Huang, J., Best, S., & Bonfield, W. (2005). Crystal imperfection studies of pure and silicon substituted hydroxyapatite using Raman and XRD. *Journal of materials science: materials in medicine*, *16*(12), 1143-1148.
69. Salamon, D., Teixeira, S., Dutczak, S. M., & Stamatialis, D. F. (2014). Facile method of building hydroxyapatite 3D scaffolds assembled from porous hollow fibers enabling nutrient delivery. *Ceramics international*, *40*(9), 14793-14799.
70. Mendez-Vilas, A., Bruque, J. M., & González-Martín, M. L. (2007). Sensitivity of surface roughness parameters to changes in the density of scanning points in multi-scale AFM studies. Application to a biomaterial surface. *Ultramicroscopy*, *107*(8), 617-625.
71. Hansson, K. N., & Hansson, S. (2011). Skewness and kurtosis: important parameters in the characterization of dental implant surface roughness—a computer simulation. *International Scholarly Research Notices*, *2011*.
72. Bagno, A., & Di Bello, C. (2004). Surface treatments and roughness properties of Ti-based biomaterials. *Journal of materials science: materials in medicine*, *15*(9), 935-949.
73. Ashraf, S., Ahmed, M. K., Ibrahium, H. A., Awwad, N. S., Abdel-Fattah, E., & Ghoniem, M. G. (2021). Nanofibers of polycaprolactone containing hydroxyapatite doped with aluminum/vanadate ions for wound healing applications. *New Journal of Chemistry*, *45*(48), 22610-22620.
74. Al-Wafi, R., Mansour, S. F., AlHammad, M. S., & Ahmed, M. K. (2021). Biological response, antibacterial properties of ZrO_2/hydroxyapatite/graphene oxide encapsulated into nanofibrous scaffolds of polylactic acid for wound healing applications. *International journal of pharmaceutics*, *601*, 120517.
75. Menazea, A. A., & Ahmed, M. K. (2020). Synthesis and antibacterial activity of graphene oxide decorated by silver and copper oxide nanoparticles. *Journal of Molecular Structure*, *1218*, 128536.

76. El-Naggar, M. E., Abu Ali, O. A., Saleh, D. I., Abu-Saied, M. A., Ahmed, M. K., Abdel-Fattah, E., & Mansour, S. F. (2022). Degradation of methylene blue using Co-dopant of Mg and Se into hydroxyapatite composite. *Luminescence*.
77. Afifi, M., Ahmed, M. K., Ibrahium, H. A., Awwad, N. S., Abdel-Fattah, E., & Alshahrani, M. Y. (2022). Improvement of physicochemical properties of ternary nanocomposites based on hydroxyapatite/CuO/graphene oxide for biomedical usages. *Ceramics International*, *48*(3), 3993-4004.
78. Díaz, M., Barba, F., Miranda, M., Guitián, F., Torrecillas, R., & Moya, J. S. (2009). Synthesis and antimicrobial activity of a silver-hydroxyapatite nanocomposite. *Journal of Nanomaterials*, *2009*.
79. Asmatulu, R., Patrick, S., Ceylan, M., Ahmed, I., Yang, S. Y., & Nuraje, N. (2015). Antibacterial polycaprolactone/natural hydroxyapatite nanocomposite fibers for bone scaffoldings. *Journal of Bionanoscience*, *9*(2), 120-126.
80. Ni, Z., Gu, X., He, Y., Wang, Z., Zou, X., Zhao, Y., & Sun, L. (2018). Synthesis of silver nanoparticle-decorated hydroxyapatite (HA@ Ag) poriferous nanocomposites and the study of their antibacterial activities. *RSC advances*, *8*(73), 41722-41730.
81. Prakash, J., Prema, D., Venkataprasanna, K. S., Balagangadharan, K., Selvamurugan, N., & Venkatasubbu, G. D. (2020). Nanocomposite chitosan film containing graphene oxide/hydroxyapatite/gold for bone tissue engineering. *International Journal of Biological Macromolecules*, *154*, 62-71.
82. El-Naggar, M. E., Abu Ali, O. A., Abu-Saied, M. A., Ahmed, M. K., Abdel-Fattah, E., & Saleh, D. I. (2022). Tailoring combinations of hydroxyapatite/cadmium selenite/graphene oxide based on their structure, morphology, and antibacterial activity. *Journal of Inorganic and Organometallic Polymers and Materials*, *32*(1), 311-325.
83. Yahia, I. S., Shkir, M., & Keshk, S. M. A. S. (2020). Physicochemical properties of a nanocomposite (graphene oxide-hydroxyapatite-cellulose) immobilized by Ag nanoparticles for biomedical applications. *Results in Physics*, *16*, 102990.
84. Govindan, R., & Girija, E. K. (2014). Drug loaded phosphate glass/hydroxyapatite nanocomposite for orthopedic applications. *Journal of Materials Chemistry B*, *2*(33), 5468-5477.

85. Beyene, Z., & Ghosh, R. (2019). Effect of zinc oxide addition on antimicrobial and antibiofilm activity of hydroxyapatite: A potential nanocomposite for biomedical applications. *Materials Today Communications*, *21*, 100612.
86. El-Naggar, M. E., Abu Ali, O. A., Saleh, D. I., Abu-Saied, M. A., Ahmed, M. K., Abdel-Fattah, E., & Mansour, S. F. (2021). Microstructure, morphology and physicochemical properties of nanocomposites containing hydroxyapatite/vivianite/graphene oxide for biomedical applications. *Luminescence*.
87. El-Naggar, M. E., Abu Ali, O. A., Abu-Saied, M. A., Ahmed, M. K., Abdel-Fattah, E., & Saleh, D. I. (2022). Tailoring combinations of hydroxyapatite/cadmium selenite/graphene oxide based on their structure, morphology, and antibacterial activity. *Journal of Inorganic and Organometallic Polymers and Materials*, *32*(1), 311-325.
88. Barabashko, M. S., Tkachenko, M. V., Neiman, A. A., Ponomarev, A. N., & Rezvanova, A. E. (2020). Variation of Vickers microhardness and compression strength of the bioceramics based on hydroxyapatite by adding the multi-walled carbon nanotubes. *Applied Nanoscience*, *10*(8), 2601-2608.
89. Rempel, S. V., Bogdanova, E. A., Valeeva, A. A., Schröttner, H., Sabirzyanov, N. A., & Rempel, A. A. (2016). Microhardness and phase composition of TiO/hydroxyapatite nanocomposites synthesized under low-temperature annealing conditions. *Inorganic Materials*, *52*(5), 476-482.
90. Bahrami, M., Fathi, M. H., & Ahmadian, M. (2015). The effect of nanobioceramic reinforcement on mechanical and biological properties of Co-base alloy/hydroxyapatite nanocomposite. *Materials Science and Engineering: C*, *48*, 572-578.
91. Wang, L., Weng, L., Song, S., Zhang, Z., Tian, S., & Ma, R. (2011). Characterization of polyetheretherketone–hydroxyapatite nanocomposite materials. *Materials Science and Engineering: A*, *528*(10-11), 3689-3696.
92. Wang, L., Nemoto, R., & Senna, M. (2004). Changes in microstructure and physico-chemical properties of hydroxyapatite–silk fibroin nanocomposite with varying silk fibroin content. *Journal of the European Ceramic Society*, *24*(9), 2707-2715.

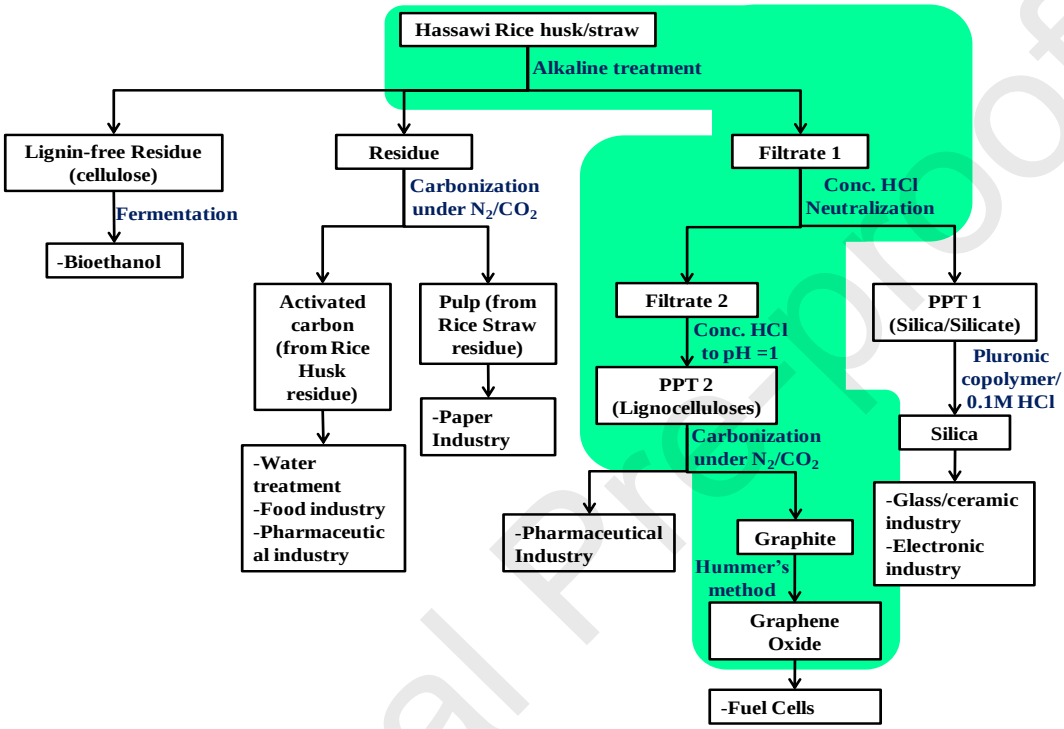

Scheme 1: Route for the production of graphite and graphene oxide from Hassawi rice biomass waste

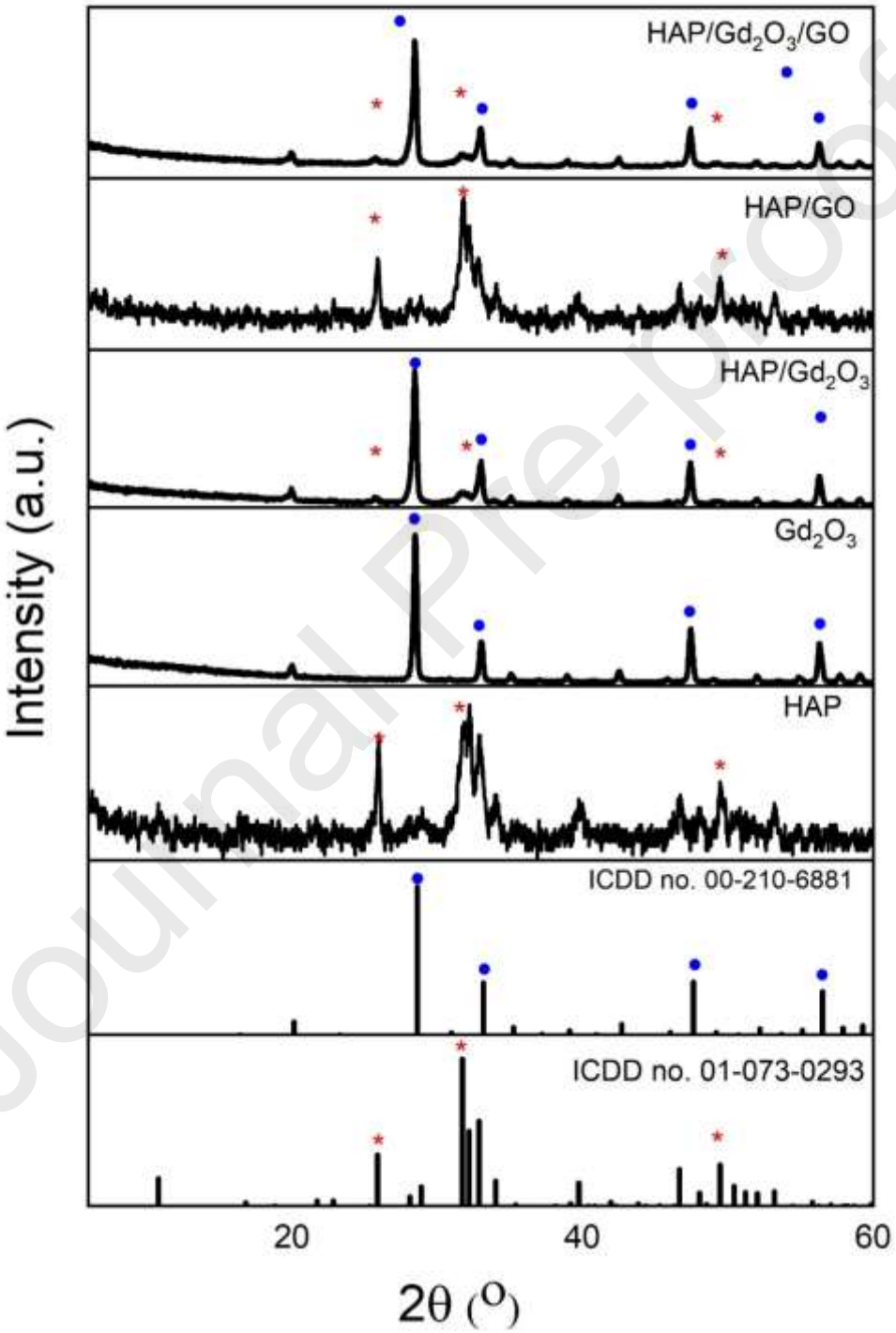

Fig 1. The XRD pattern from 6^{o} to 60^{0} for HAP, Gd_2O_3, HAP/ Gd_2O_3, HAP/GO, and HAP/ Gd_2O_3/GO. (*) refers to the main peaks of HAP, while (·) refers to the characteristic peaks of Gd_2O_3.

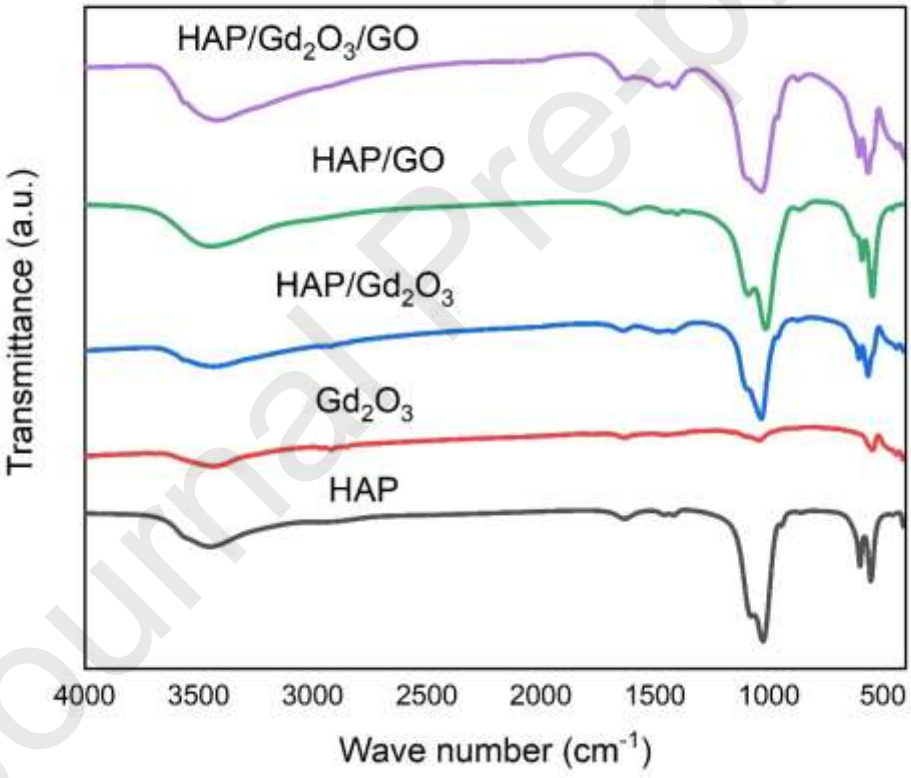

Fig 2. FT-IR spectra of all compositions in the range of 4000-400 cm^{-1}.

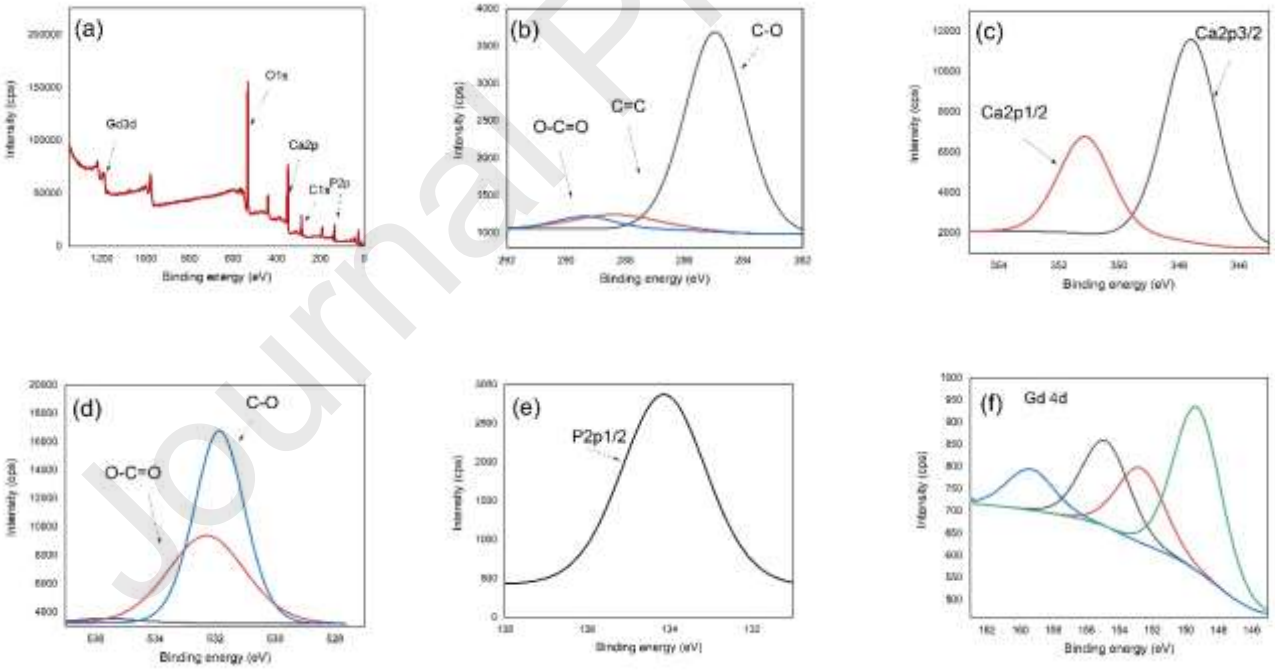

Fig 3. (a) XPS investigation of TNC survey, while (b-f) are XPS analysis of C1s, Ca2p, O1s, P2p, S2p, and Gd4d respectively.

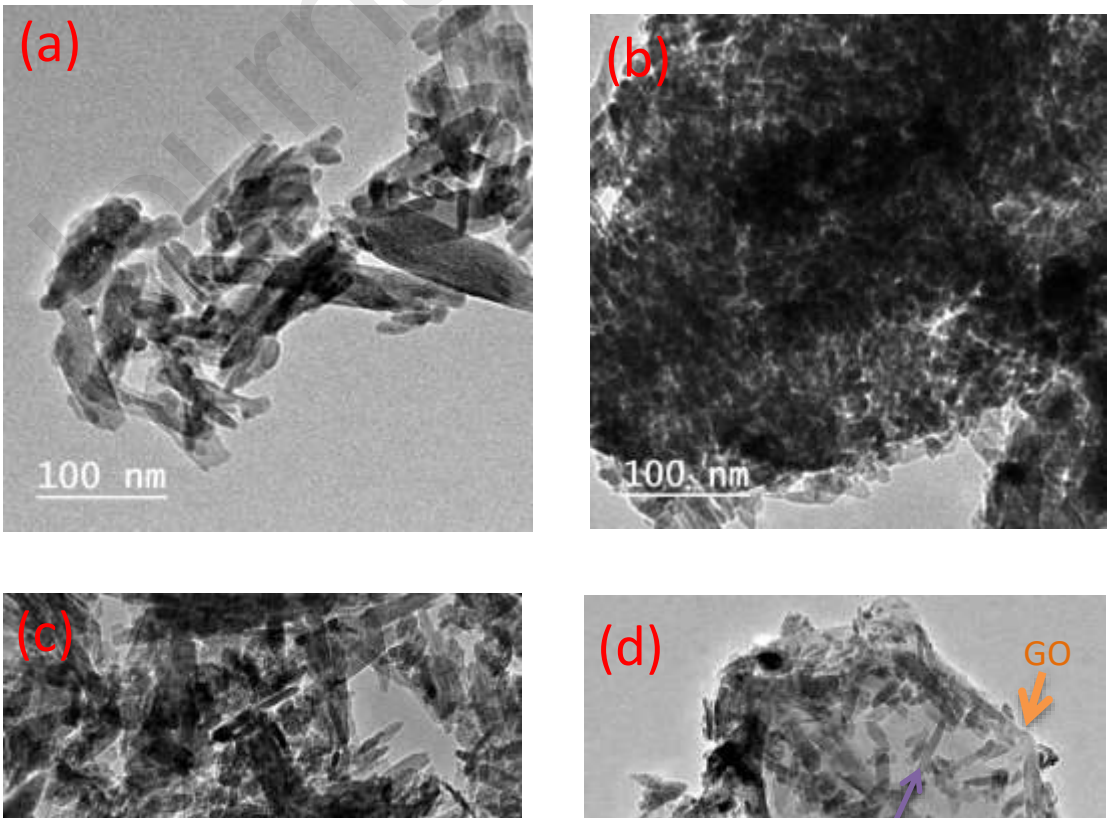

Fig 4. TEM micrographs of (a) HAP (b) Gd_2O_3, (c) HAP/ GO (d) HAP/ Gd_2O_3/GO ternary-nanocomposite.

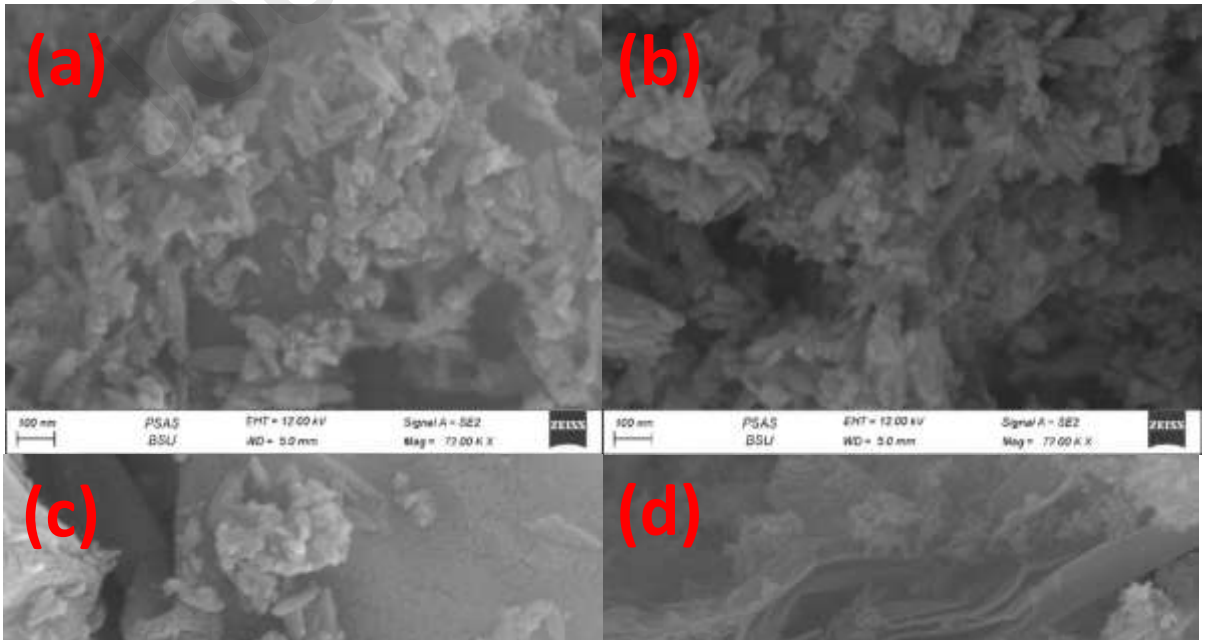

Fig 5. FESEM scan, which shows the morphology of (a) HAP, (b) HAP/ Gd_2O_3 (c) HAP/ GO, and (d) HAP/ Gd_2O_3/GO TNC.

Fig 6. The obtained roughness micrographs of FESEM scanning, where (a) HAP, (b) HAP/ Gd_2O_3 (c) HAP/ GO, and (d) HAP/ Gd_2O_3/GO nanocomposites respectively.

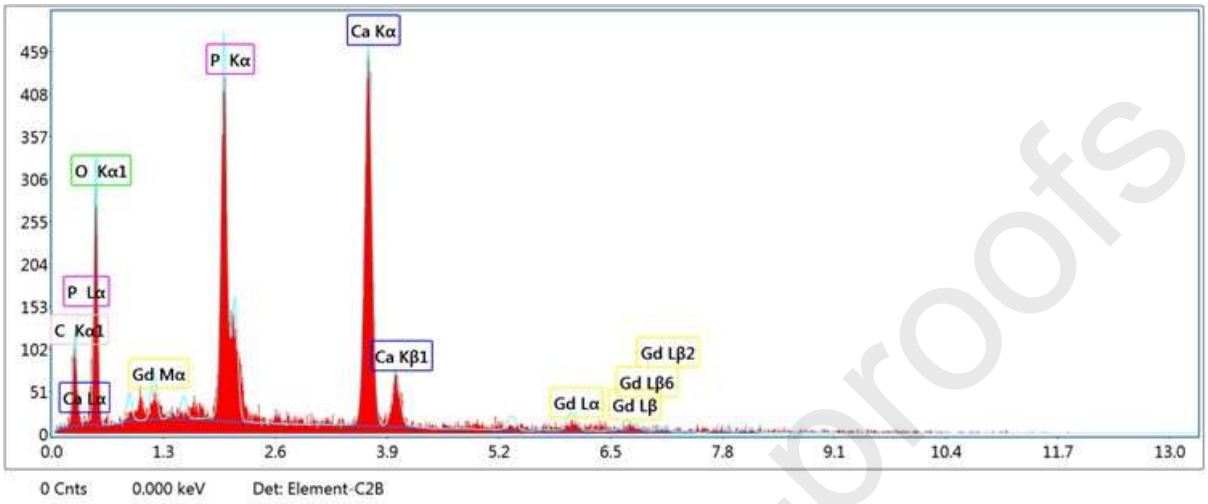

Fig 7. The EDX analysis based on SEM for HAP/ Gd_2O_3/GO nanocomposite.

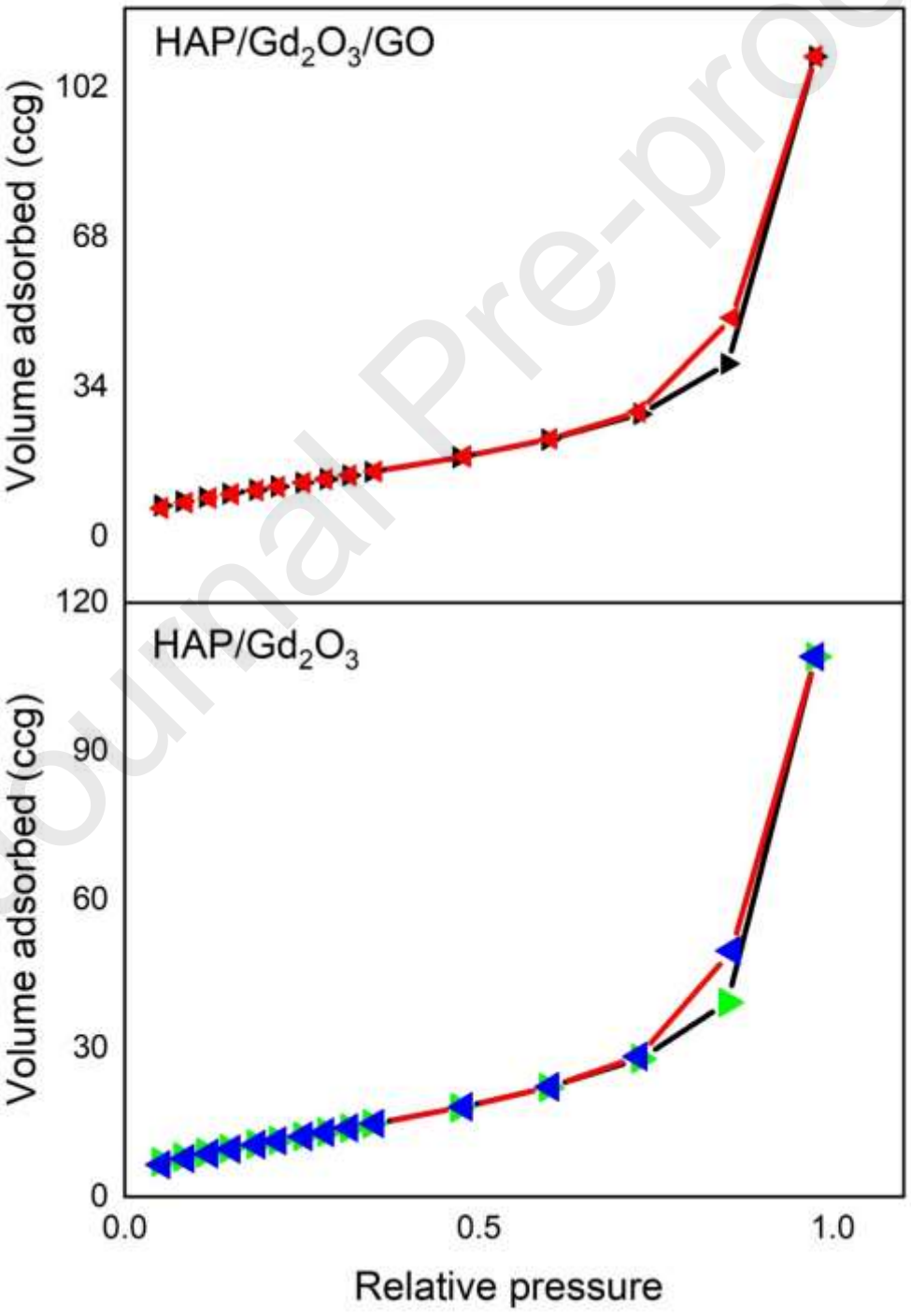

Fig. 8 The relative pressure relation with the volume adsorbed, where the black line is the adsorption and the red line is desorption.

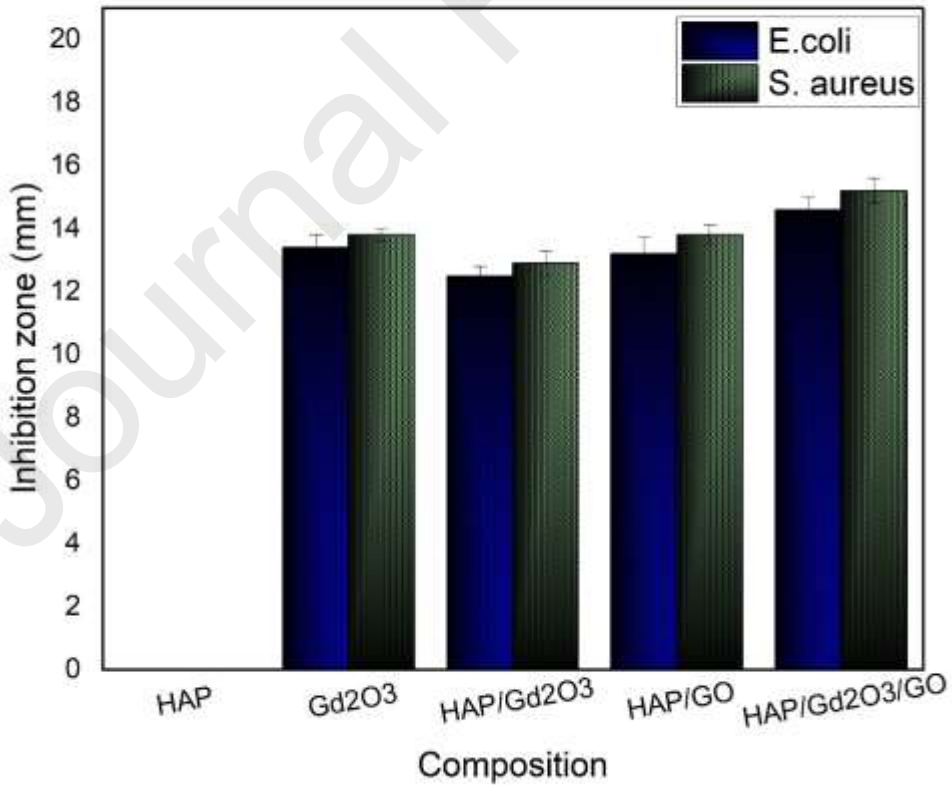

Fig 9. The inhibition zone of the anti-bacterial behavior of the NCs against E.coli and S. aureus

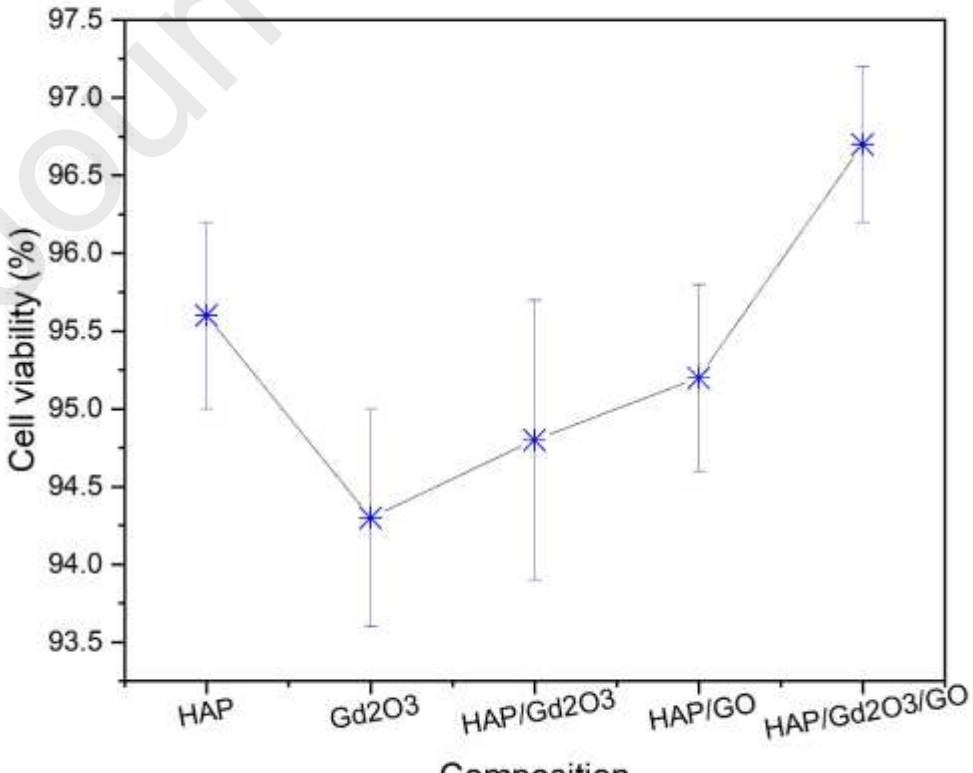

Fig 10. Cell viability of the composites toward the human osteoblast cells in vitro.

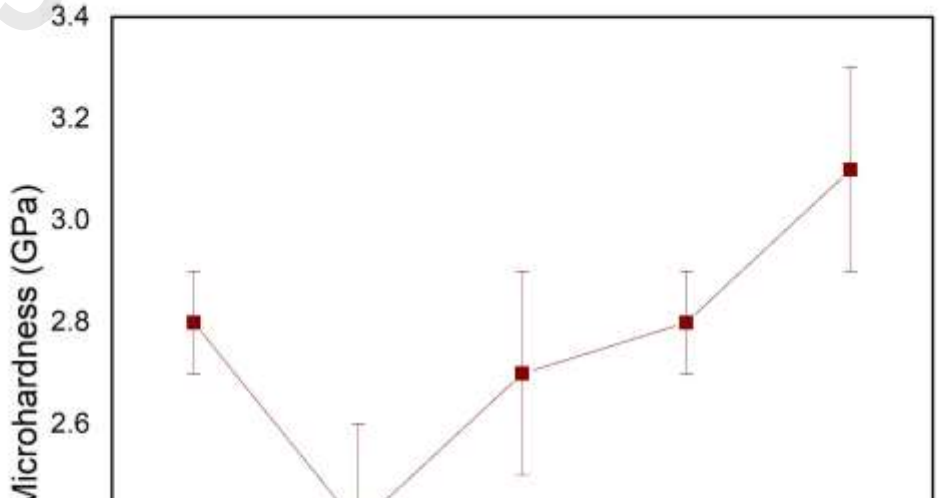

Fig. 11 The microhardness investigation with the standard errors for all compositions.